11-23-2021

Macro and micro coupling analysis of cone penetration test: methodology and application

Chang-hong WANG

Dao-fei TANG

Kun WANG

Zhao-xin WU

Custom Citation
WANG Chang-hong, TANG Dao-fei, WANG Kun, WU Zhao-xin. Macro and micro coupling analysis of cone penetration test: methodology and application[J]. Rock and Soil Mechanics, 2021, 42(7): 1815-1827.

Macro and micro coupling analysis of cone penetration test: methodology and application

WANG Chang-hong,   TANG Dao-fei,   WANG Kun,   WU Zhao-xin

Department of Civil Engineering, School of Mechanics and Engineering Sciences, Shanghai University, Shanghai 200444, China

Abstract: Although cone penetration test (CPT) is an in-situ test method to obtain conventional geotechnical properties accurately, CPT data cannot be directly   linked to macro constitutive model parameters. The principal reason is that the comprehensive studies on the macro-micro penetration mechanism. Based on the cylindrical (cone) cavity expansion theory, a macro and micro coupling simulation method for the CPT process is established. Firstly, based on the cavity expansion theory, the relationships among the cone resistance, sleeve friction and the cavity limit pressure are derived. Secondly, the numerical triaxial compression tests with the same dimensions on the Shanghai ②₁ silty clay in the shallow bearing layer are performed by both the maco and the micro simulation methods. The conversion formulas that relate the macro perfectly elastoplastic model (i.e., Mohr-Coulomb model) parameters to the micro linear parallel-bond model parameters have been proposed and implemented in the commonly used commercial software FLAC³ᴰ. The macro-micro conversion formulas are validated by the CPT data on Shanghai ②₁ silty clay and ⑤₁₋₁ gray clay. Finally, the discrepancies between the theoretical solution, numerical modelling results and the CPT measurements of cone resistance, sleeve friction and cavity limit pressure on the Shanghai ②₁ silty clay are analyzed from a macro perspective. The distribution of soil displacement and the contact force chain are presented and discussed from the micro perspective. The discrepancies between the theoretical solutions and the CPT measurements of the cavity limit pressure, cone resistance and sleeve friction are 1.30%, 0.45% and 0.77%, respectively. The discrepancies between the macro and micro coupling simulation results and the CPT measurements of the cavity limit pressure, cone resistance, sleeve friction and pore pressure are 9.68%, 2.99%, 9.19% and 8.42%, respectively. It indicates that the macro and micro coupling numerical modelling results are not only in agreement with the cavity expansion theory-based theoretical solutions and the CPT measurements, but also the effect of pore pressure can be simulated. The proposed macro and micro coupling simulation provides insight into the CPT mechanism and the approach to estimating the macro-micro parameters of the specific constitutive models.

Keywords: cone penetration test; cavity expansion theory; macro and micro mechanics; coupling analysis

1 Introduction

Cone penetration test (CPT) provides information on the complex stress states and the variable geotechnical parameters of the subsurface soils, such as total penetration resistance p_s, cone resistance q_c, sleeve friction f_s, and pore pressure u. Over recent decades, substantial research efforts have been devoted to investigating the fundamental mechanism and interpreting the measurements of cone penetration tests. The investigation approaches can be classified into three main categories. (1) Regression analysis: According to the results of in-situ geotechnical tests and laboratory tests, empirical formulas are established by regression analysis. For instance, Liu et al.[1] summarized the empirical formulas which relate the shear strength and coefficient of permeability of cohesive soils and cohesionless soils under various stress states to CPT data. Duan et al. [2] concluded that the shear wave velocity has a strong correlation with the undrained shear strength based on the CPT measurements on Jiangsu clay. The

empirical formulas based on the regression analysis are applicable to a specific regional soil; on the other hand, those formulas cannot be extended for soils in other regions and do not indicate the underlying mechanism of CPT. (2)Theoretical analysis: Based on the spherical or cylindrical cavity expansion theory in combination with perfectly elastoplastic model and modified Cam−Clay model which account for the softening and dilation behavior of geomaterials, the calculation formulas for stress field, displacement field and cavity limit pressure are derived (Chen et al.[3], Qiu et al.[4]). Typically, theoretical analysis estimates with simplifications for q_c, f_s (or p_s) without the influence of pore pressure. (3)Numerical simulation: The approaches mainly include finite element method (FEM) (e.g., Geng et al.[5], Ahmadi et al.[6]) and discrete element method (DEM) (e.g., Jiang et al. [7], Zou et al. [8]). Compared with theoretical analysis, numerical modelling is capable of simulating the complex behavior of

geomaterials with various types of boundary conditions imposed. The influence of pore pressure can be simulated as well. Due to the basic characteristics of geomaterials, such as fragmented and multiphase properties, the macroscopic deformation and failure of the soil are associated with the microscopic discontinuous mechanical behavior, i.e., change in internal microstructure and fracturing. When the CPT process is modelled using the FEM, the physical mesh will become so distorted that the simulations could crash prematurely. Therefore, it is a research trend to use the DEM to simulate the CPT process, and the simulation results are more consistent with the test data. Due to the limitation of the size and quantity of soil particles, there are challenges regarding the macro−micro conversion of geotechnical parameters and computation efficiency. Deng et al.[9] provided an effective modelling strategy to reduce the limitation due to the limited number of particles, in which small-sized particles are used in the near field and particles with the gradually increasing sizes are used in the far field. In addition, the FEM-DEM coupled simulation method has become a new approach to reduce the limitation due to particle size and quantity (Ma et al. [10]).

In summary, CPT is an in-situ testing method used to accurately obtain conventional geotechnical parameters. However, the studies on the direct conversion from the CPT data to geotechnical macro constitutive model parameters (i.e., a class of fine geotechnical parameters) remain limited. Moreover, the research on the cone penetration mechanisms from macro and micro perspectives is insufficient. Based on the cylindrical (cone) cavity expansion theory and the Mohr-Coulomb yield criterion, a macro and micro coupling numerical modelling approach for cone penetration test process is proposed. The discrepancies between the theoretical solution, numerical modelling results and the CPT measurements of cone resistance, sleeve friction and cavity limit pressure are analyzed from a macro perspective. Additionally, the distributions of soil particle displacements and the contact force chain are presented and discussed from the micro perspective.

2 Cylindrical (cone) cavity expansion theory

According to the cylindrical cavity expansion theory, the Mohr-Coulomb yield criterion is used to describe the elastic-plastic mechanical characteristics of the soil, and the stress and displacement solutions during the expansion of the cylindrical cavity are obtained. The static balance equation of cone resistance is established, and the static equilibrium relationship between cone

resistance, sleeve friction and limit expansion stress are derived.

2.1 Cylindrical cavity expansion theory

Cylindrical cavity expansion theory adopts the perfectly elastoplastic constitutive model, i.e., Mohr-Coulomb yield criterion. The stress and displacement in the elastic and plastic zones are estimated. Then, the force equilibrium relationship between the cavity limit pressure and the cone resistance is derived.

2.1.1 Basic assumptions

Figure 1 illustrates the calculation model for the cylindrical cavity expansion theory in the infinite space in the cylindrical polar coordinate system. The soil is assumed to be homogeneous and isotropic and obey the elastoplastic constitutive model with the Mohr-Coulomb yield criterion. The cylindrical cavity expands from its initial cavity radius a_0 to the current radius a, when the internal pressure increases from p_0 to the cavity limit pressure p_a. During the cavity expansion process, r_0 is the radius at a point before the cylindrical cavity expands, r is the radius at which the cylindrical cavity expands. The cylindrical cavity is surrounded by a plastic zone, which is encompassed by the outer elastic zone. The radial location of the soil particle at the elastic-plastic boundary changes from b_0 to b after the cavity expands. p_b is the stress at the current elastic-plastic boundary, u_r is the radial displacement of the soil particle at the radial location r from the center of the cylindrical cavity, u_b is the radial displacement of the elastic-plastic boundary after the cavity expansion.
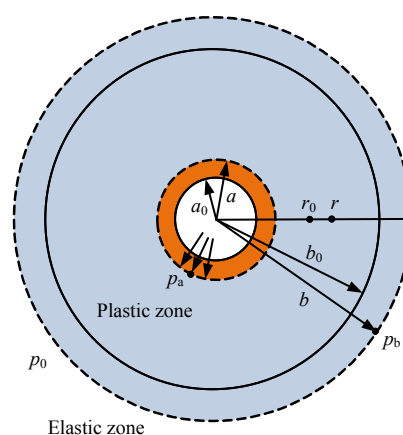

Fig. 1 Schematic illustration of cylindrical cavity expansion theory-based model[3]

2.1.2 Stress and displacement solutions

Li [11] obtained the stress field in the plastic zone of a cylindrical cavity and the relative radial displacement of the elastic-plastic boundary based on the theory of elastic and plastic mechanics:

$$
\left.
\begin{array}{l}
\sigma_r = \left(p_a + \dfrac{B}{1-A} \right)\left(\dfrac{a}{r} \right)^{1-A} - \dfrac{B}{1-A} \\[2mm]
\dfrac{u_b}{b} = \dfrac{p_b - p_0}{2G_0}
\end{array}
\right\} \tag{1}
$$

where σ_r is the radial stress; $A = \dfrac{1-\sin\varphi}{1+\sin\varphi}$; $B =$

$\dfrac{2c\cos\varphi}{1+\sin\varphi}$; E is the elastic modulus; v is Poisson's

ratio; c is the cohesion; and φ is the internal friction angle.

Based on the Mohr-Coulomb yield criterion, substituting the stress at the elastic-plastic boundary $\sigma_{r=b} = p_b$ into Eq. (1), the cavity limit pressure can be rewritten as

$$
p_a = \left(p_b + \dfrac{B}{1-A} \right)\left(\dfrac{b}{a} \right)^{1-A} - \dfrac{B}{1-A} \tag{2}
$$

Chen et al.[3] obtained the ratio of the elastic-plastic boundary radius b to the cavity radius a after expansion according to the force equilibrium conditions of the cylindrical cavity expansion:

$$
\dfrac{b}{a} = \sqrt{\dfrac{\left(\dfrac{a_0}{a}\right)^2 - 1}{\left(\dfrac{p_b - p_0}{2G_0}\right)^2 - \dfrac{p_b - p_0}{G_0}}}, \text{ for } \dfrac{a_0}{a} \leqslant 1 - \dfrac{p_b - p_0}{2G_0} \tag{3}
$$

2.2 Static force equilibrium

It is assumed that static force equilibrium conditions of the cylindrical cavity expansion remain satisfied during the cone penetration process. The relationships among the sleeve friction f_s, the cone resistance q_c and the radial stress σ_r are developed on the basis of the cylindrical cavity expansion theory. The force equilibrium diagram is shown in Fig.2.
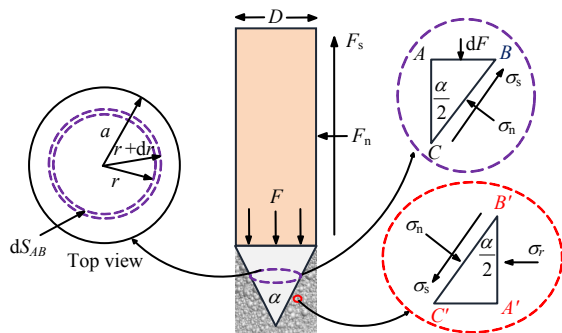

Fig. 2 Force equilibrium diagram between cylindrical cavity pressure and cone resistance

2.2.1 Cavity limit pressure and sleeve friction

The penetrometer diameter is D, and $D=2a$ for

cone penetration test process. The lateral area of the friction sleeve is S, and the coefficient of friction between the soil and the friction sleeve is μ. The cone apex angle is α, and the total cone resistance is F. The radial force F_n and the friction force F_s acting on the friction sleeve are

$$
\left.
\begin{array}{l}
F_n = S\sigma_{r=a} = SP_a \\
F_s = \mu F_n = \mu SP_a
\end{array}
\right\} \tag{4}
$$

Thus, the sleeve friction f_s is

$$
f_s = \dfrac{F_s}{S} = \dfrac{\mu F_n}{S} = \dfrac{\mu SP_a}{S} = \mu P_a \tag{5}
$$

2.2.2 Cavity limit pressure and cone resistance

As shown in Fig.2, for an arbitrary point with the radial location of r on the cone surface, the horizontal projection area and the oblique area at the point with an infinitesimal increment dr are

$$
\left.
\begin{array}{l}
dS_{AB} = 2\pi r\, dr \\[2mm]
dS_{BC} = \dfrac{dS_{AB}}{\sin\dfrac{\alpha}{2}}
\end{array}
\right\} \tag{6}
$$

The static force equilibrium in the vertical direction can be expressed as

$$
dF = \sigma_n dS_{BC} \sin\dfrac{\alpha}{2} + \sigma_s dS_{BC} \cos\dfrac{\alpha}{2} \tag{7}
$$

where σ_n is the normal stress; σ_s is the shear stress. When $\sigma_s = \mu\sigma_n$, the cone resistance q_c is

$$
q_c = \dfrac{F}{A} = \dfrac{2}{R^2}\left(1 + \dfrac{\mu}{\tan\dfrac{\alpha}{2}} \right)\int_0^a \sigma_n r\, dr \tag{8}
$$

The static force equilibrium analysis in the horizontal direction of the soil surrounding the cone leads to

$$
\sigma_r dS_{A'B'} = \sigma_n dS_{B'C'}\cos\dfrac{\alpha}{2} - \sigma_s dS_{B'C'}\sin\dfrac{\alpha}{2} \tag{9}
$$

Based on the geometric relationship between $dS_{A'B'}$ and $dS_{B'C'}$ that is the same as that between dS_{AB} and dS_{BC}, Eq. (9) can be rewritten as

$$
\sigma_n = \dfrac{\sigma_r}{\left(1 - \mu\tan\dfrac{\alpha}{2} \right)} \tag{10}
$$

Substituting Eq. (10) into Eq. (8) leads to

$$
q_c = \dfrac{2}{R^2} \cdot \dfrac{\left(1 + \dfrac{\mu}{\tan\dfrac{\alpha}{2}} \right)}{\left(1 - \mu\tan\dfrac{\alpha}{2} \right)} \int_0^a \sigma_r r\, dr \tag{11}
$$

Using the typical CPT cone apex angle $\alpha = 60°$, Eq. (11) can be rewritten as

$$q_{c} = \frac{2}{R^{2}} \frac{(1+\sqrt{3}\mu)}{\left(1-\frac{\sqrt{3}}{3}\mu\right)} \int_{0}^{a} \sigma_{r} r \mathrm{d}r \qquad (12)$$

When the radius of the cavity expands to a, the radial stress at the cavity wall $\sigma_{r}\big|_{r=a}$ reaches the cavity limit pressure p_{a}. Thus, q_{c} can be simplified as

$$q_{c} = \frac{(1+\sqrt{3}\mu)}{\left(1-\frac{\sqrt{3}}{3}\mu\right)} p_{a} \qquad (13)$$

Based on the cylindrical (cone) cavity expansion theory in combination with the perfectly elastoplastic constitutive model with Mohr-Coulomb yield criterion, the static force equilibrium relationships are established, which relate the geotechnical parameters to the CPT measurements (i.e., cone resistance and sleeve friction). However, the cylindrical (cone) cavity expansion theory-based solutions have limitations. Essentially, the cone penetration into the soil is a microscopic, three-dimensional and dynamic process. The three-dimensional macro and micro coupling numerical modelling method proposed in the current study is devoted to investigating the cone penetration mechanism, macro and micro coupling mechanism, and the selection and conversion of the CPT macro and micro parameters.

3 Macro and micro coupling numerical simulation method

The numerical modelling of the cone penetration test adopts the coupled numerical simulation code in FLAC³ᴰ 6.0 [12] (fast Lagrangian analysis of continua in 3 dimensions). The discrete element method (DEM) based software PFC³ᴰ 5.0 [13] is built in the finite difference method (FDM) based software FLAC³ᴰ 6.0. Thus, the macro and micro coupling numerical modelling method can be implemented and be capable of simulating both the macro continuous and micro discontinuous soil behavior.

3.1 Macro and micro coupling mechanism

The coupling between PFC³ᴰ and FLAC³ᴰ in previous versions has limitations due to data loss and low accuracy. In FLAC³ᴰ version 6.0, the two-way coupling of solid elements and discrete soil particles is implemented through the wall facets in the coupling simulation domain as shown in Fig.3. The wall facets are generated on the surface of the solid element and shares nodes with the solid element. The wall facet is composed of triangular surfaces, where the velocity and force at the nodes vary with respect to time. The contact force and moment on the wall facet generated by soil particles transmit to the solid element through the wall facet,

which changes the force and displacement in the solid elements, and vice versa. F_{n} and F_{s} are the normal component and tangential component of the equivalent nodal force.
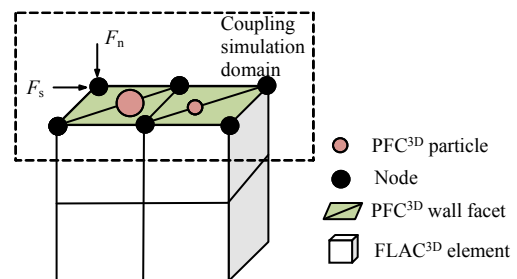

Fig. 3 Schematic illustration of FLAC³ᴰ and PFC³ᴰ coupling simulation mechanism

3.2 Macro and micro mechanical constitutive models

In order to coordinate the force and displacement of the macro and the micro model, it is necessary to develop the parameter conversion formulas between the macro and the micro mechanical constitutive model. For the sake of convenience, the macro and micro constitutive models are chosen based on the model applicability, the number of model parameters and the feasibility of macro and micro model parameter conversion.

3.2.1 Microscopic contact model

The linear parallel-bond model is suitable for modelling geomaterials with bonding strength, where parallel bonds transfer forces and moments between particles. When the parallel bond is disconnected, the model degenerates to a linear model. Fig.4 illustrates the linear parallel-bond model, where $\overline{F}^{n}$ and $\overline{F}^{s}$ are the normal and tangential component of contact forces in the parallel bond; $\overline{M}^{n}$ and $\overline{M}^{s}$ are the normal and tangential component of bending moments in the parallel bond. The parallel-bond model includes the parameters of the linear model and those of the parallel bond. According to the previous studies on the numerical simulation of cone penetration tests by the parallel-bond model[12, 14], the effective modulus E^{*} and stiffness ratio κ^{*} of the linear model are equal to the effective modulus $\overline{E}^{*}$ and stiffness ratio $\overline{\kappa}^{*}$ of the parallel bond, i.e., $E^{*} = \overline{E}^{*}$, $\kappa^{*} = \overline{\kappa}^{*}$. The parameters of the linear parallel-bond model include the effective modulus E^{*}, the stiffness ratio κ^{*}, the micro cohesion c^{*}, and the micro internal friction angle φ^{*}.

3.2.2 Macroscopic constitutive model

Numerous constitutive models have been proposed in the literature, such as the Drucker-Prager, Mohr-Coulomb model, the modified Cam-Clay model, the small strain model, and the unified hardening model (Yao [15]) that can model the soil's complex behavior, such as shear contraction or dilation, hardening or

softening, over-consolidation and microstructure properties. The Mohr-Coulomb model has been widely used in geotechnical engineering because of its fewer model parameters and capacity of modelling the strength characteristics and failure behavior of geomaterials. The main parameters of the perfectly elastoplastic model with the Mohr-Coulomb yield criterion include elastic modulus E, Poisson's ratio v, cohesion c and internal friction angle φ. The above model parameters are associated with those of the micro linear parallel-bond model. Therefore, the Mohr-Coulomb model can be used as the macro constitutive model, considering the model applicability, the number of parameters and the feasibility of model parameter conversion.
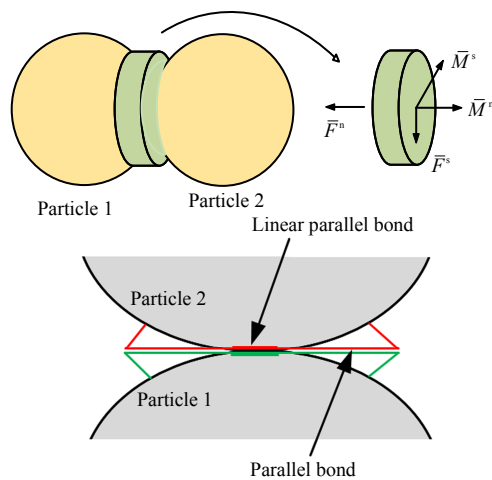

Fig. 4 Schematic illustration of the linear parallel-bond model[13]

Based on the CPT data in a construction field, the conversion formulas of model parameters between macro and micro constitutive models are investigated in the next section. Moreover, the soil's both macro continuous behavior and micro discontinuous behavior during the cone penetration process are studied by performing the macro and micro coupling numerical simulation.

4 Case study

The geological strata are soft silty soil layers with poor mechanical strength from the ground surface to the depth of about 20 m in Shanghai region, except for the ② layer of silty clay and the ⑤$_{1-1}$ layer of gray clay. The groundwater table in Shanghai region is shallow,

the fluctuation of which affects the mechanical properties of the soil, such as shear strength and volume change. For the shallow foundation design, the ②$_1$ layer of silty clay is typically selected as the bearing layer. Therefore, conversion formulas between the macro and micro constitutive model parameters are developed by conducting the numerical triaxial compression tests on the ②$_1$ layer of silty clay with the same dimensions in FLAC^{3D} and PFC^{3D}. Then, the conversion formulas are validated by comparing the simulation results with PFC^{3D} with both the cavity expansion theory-based solutions and measured values of cone penetration test on Shanghai ②$_1$ silty clay and ⑤$_{1-1}$ gray clay. Finally, the discrepancies between the theoretical solution, numerical modelling results and the CPT measurements of cone resistance, sleeve friction and cavity limit pressure on the Shanghai ②$_1$ silty clay are analyzed from a macro perspective. The distribution of soil displacement and the contact force chain are presented and discussed from the micro perspective.

4.1 Project overview

Gubei New Area is located about 5 km east of Shanghai Hongqiao International Airport. Its location and subsurface soil profile of the construction site are shown in Fig.5. From the top to bottom strata, there are ①$_1$ miscellaneous fill, ①$_2$ hidden creek fill, ②$_1$ silty clay, ②$_2$ gray-yellow clay, ③ gray muddy silty clay, ④ gray silty clay, and ⑤$_{1-1}$ gray clay. The depth of the groundwater table is about 1 m. The thickness the shallow bearing layer, i.e., the ②$_1$ layer of silty clay is about 1 m. Based on the comprehensive field survey and engineering judgment, the conventional geotechnical parameters are listed in Table 1. The in-situ cone penetration test results on ②$_1$ layer of silty clay and ⑤$_{1-1}$ layer of gray clay are shown in Table 2.
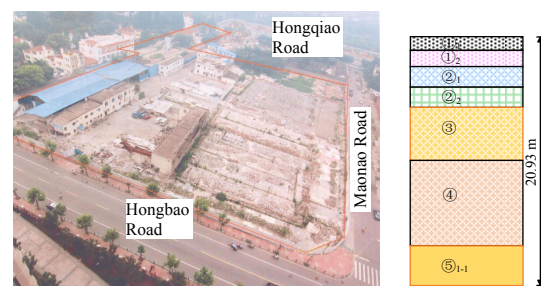

Fig. 5 The location and the subsurface soil profile of the construction site

Table 1 Computational parameters of the numerical model

| Soil layer	Constitutive model	Unit weight γ/(kN·m^{-3})	Poisson's ratio v	Cohesion c/kPa	Internal friction angle φ/(°)	Elastic Modulus E/MPa	Saturated coefficient of permeability k_s/(cm·s^{-1})	Initial stress p_0/kPa	Particle size d/mm
②$_1$ silty clay	Mohr-Coulomb	18.9	0.30	24	17.5	15.45	1.6×10^{-6}	102	0.005
⑤$_{1-1}$ gray clay	Mohr-Coulomb	17.3	0.33	14	16.0	9.42	—	200	0.005
Probe	Linear elasticity	78.0	0.25	1 000	—	2.10×10^5	—	—	—

Table 2 CPT data of the construction project

Soil layer	Cone resistance q_c /MPa			Sleeve friction f_s /kPa			Pore pressure u / kPa		
	Mean	Maximum	Minimum	Mean	Maximum	Minimum	Mean	Maximum	Minimum
②₁ silty clay	0.67	1.27	0.39	25.9	60.5	17.2	1.9	3.4	1.37
⑤₁₋₁ gray clay	0.74	0.79	0.72	12.2	16.9	11.3	—	—	—

4.2 Numerical model and boundary conditions for cone penetration test

The boundary effect needs to be minimized, when the numerical modelling on cone penetration test is performed. Gui et al.[16] developed the centrifuge modelling technique of cone penetration process and found that the influence of the boundary effect can be significantly reduced when the size of the model box is 20 times greater than the cone diameter. Jiang et al. [17] concluded that the number of particles in contact with the cone should be greater than 13 to obtain stable measurement of cone tip resistance in the discrete element simulation. Geng et al.[5] conducted numerical modelling of cone penetration tests at various penetration rates and found that the penetration rate has negligible effect on the cone resistance. Considering the accuracy and efficiency of the numerical simulation, the model dimensions are shown in Fig.6 and Table 3. The model has 57,099 elements and around 110,000 particles. The particle

diameters are generated in the range of 2.2−3.6 mm in accordance with the measured grain size distribution curve of the studied soils. The cone penetration speed is 0.25 mm/s. The boundary between the DEM element in PFC³ᴰ and the FDM element in FLAC³ᴰ is permeable. The wall facets in FPC³ᴰ are developed on the boundary between DEM and FDM elements and the surface of the cone.

(a) Numerical model dimensions of cone penetration test

(b) Coupling simulation via the PFC³ᴰ wall facets
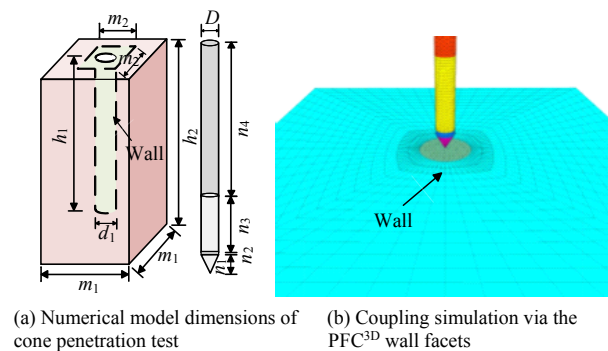
Fig. 6 Numerical model of the cone penetration test

Table 3 Numerical model dimensions of cone penetration test

Filling height of internal particles h_1 /m	Filling diameter of internal particle d_1 /m	Model height h_2 /m	Model length m_1 /m	Wall length m_2 /m	Penetrometer diameter D /m	Cone height n_1 /m	Pore pressure filter length n_2 /m	Friction sleeve length n_3 /m	Remaining penetrometer length n_4 /m
0.8	0.10	1.0	0.76	0.2	0.036	0.03	0.01	0.134	0.556

4.3 The conversion formulas between macro and micro constitutive model parameters

According to references [18−19], numerous macro and micro studies focus on the macro and micro characteristics of rock samples through uniaxial, biaxial, and Brazilian split tests. The set of micro constitutive model parameters is typically determined by the simulation results which are in consistent with physical model test results. Research on the conversion of macro and micro model parameters in cohesive soils is limited. Chen et al. [20] conducted numerical simulations of biaxial tests on cohesive soils and established the relationship between the macro and micro internal friction angles. Zhou et al. [21] carried out numerous plane biaxial compression tests on cohesive soils and related the macro shear strength parameters (internal friction angle, cohesion) to the micro parameters of the particle flow by the nonlinear fitting method. Basically, the existing studies use the linear contact model in combination with Mohr-Coulomb yield criterion to investigate the relationships between the macro and micro model

parameters. However, there are few studies which focus on the properties of clays using the parallel-bond model combined with Mohr-Coulomb yield criterion.

Considering that there may be differences between two−and three−dimensional numerical modelling results as well as other influencing factors such as model size, particle size, and confining pressure, the macro and micro numerical triaxial compression test models are developed (see Fig.7), in order to obtain the conversion formulas between the macro and micro model parameters for the cone penetration modelling shown in Fig.6. The numerical model has a height of 1.0 m and a diameter of 0.2 m. According to the research findings by Su et al. [22], the ratio of the model height L to the average particle radius R (i.e., L/R) does not affect the peak strength and the corresponding strain, Young's modulus and Poisson's ratio, if the ratio is greater than 125. Thus, the ratio L/R in the numerical model is taken as 200, and consequently the particle diameter in the micro triaxial compression test model is less than 16 mm. Taking the efficiency and accuracy of numerical simulation into

account, the average particle sizes in the micro model are divided into five groups, i.e., 8, 10, 12, 14 and 16 mm.
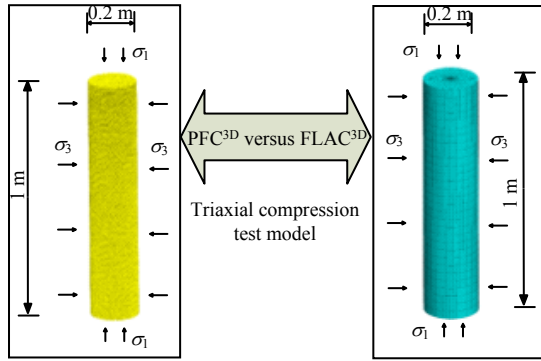

Fig. 7　3D Triaxial compression test model

Taking the ②₁ layer of silty clay in the shallow bearing layer in Shanghai area as an example, the peak stress and the corresponding strain by the macro and micro modelling are compared using various sets of macro and micro model parameters. When the macro and micro triaxial compression tests modelling produce the same peak stress and strain with the error less than 5%, the two sets of macro and micro model parameters are considered equivalent. Fig.8 is one set of both macro and micro modelling on the triaxial compression comparison test under confining pressure of 67 kPa.
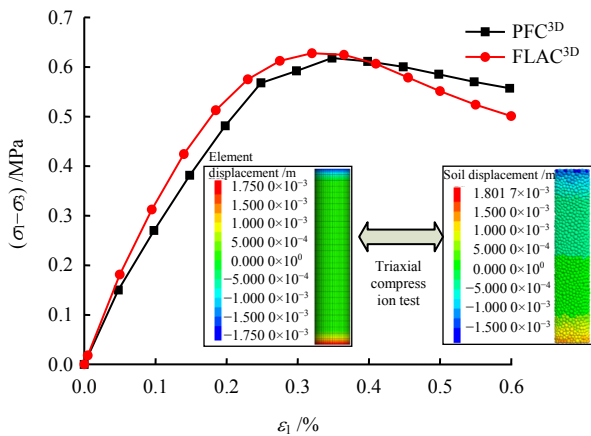

Fig. 8　Stress−strain curves of triaxial compression tests at the confining pressure of 67 kPa using FLAC³ᴰ and PFC³ᴰ

Through the comparison of multiple sets of numerical experiment results, the equivalent macro and micro model parameters are obtained, and the parameter conversion formulas are developed by nonlinear fitting. In order to develop the dimensionless parameters, the reference stress $\sigma_{\text{ref}} = 1\,\text{kPa}$, the reference particle diameter $d_{\text{ref}} = 1\,\text{mm}$, the reference cohesion $c_{\text{ref}} = 1\,\text{kPa}$, and the reference Young's modulus $E_{\text{ref}} = 1\,\text{MPa}$.

Table 4 shows the variation range of macro model parameters and particle sizes, which includes 31

combinations (i.e., 6 different confining pressures and 5 different particle sizes).

Table 4　Variation range of macro constitutive model parameters and particle sizes in numerical modelling

E /MPa	c /kPa	φ /(°)	v	σ_3 /kPa	d /mm
6	8	8	0.150	67	8
9	12	12	0.225	133	10
12	16	16	0.300	200	12
15	20	20	0.375	267	14
18	24	24	0.450	333	16
—	—	—	—	400	—

Through the comparison of the simulation results by FLAC³ᴰ and PFC³ᴰ, the conversion formulas between macro and micro model parameters are developed. The relationships between macro and micro model parameters are plot in Figs.9−12. The conversion formulas between the macroscopic Young's modulus E and the micro effective modulus E^* are

$$\left.\begin{aligned} E &= 0.939E^{*0.933}\kappa^{*-0.022}\left(\frac{c^*}{c_{\text{ref}}}\right)^{0.079}\left(\frac{\sigma_3}{\sigma_{\text{ref}}}\right)^{-0.308}\left(\frac{d}{d_{\text{ref}}}\right)^{-0.037\,3} \\ E^* &= 0.73E^{1.012}\left(\frac{\sigma_3}{\sigma_{\text{ref}}}\right)^{0.318}\left(\frac{d}{d_{\text{ref}}}\right)^{0.515} \end{aligned}\right\} \tag{14}$$

The conversion formulas between macro Poisson's ratio v and micro stiffness ratio κ^* are

$$\left.\begin{aligned} v &= 0.02\left(\frac{E^*}{E_{\text{ref}}}\right)^{0.701}\kappa^{*0.06}\left(\frac{c^*}{c_{\text{ref}}}\right)^{0.107}\left(\frac{\sigma_3}{\sigma_{\text{ref}}}\right)^{-0.101}\left(\frac{d}{d_{\text{ref}}}\right)^{-0.199} \\ \kappa^* &= 0.016\left(\frac{E}{E_{\text{ref}}}\right)^{1.605}\left(\frac{\sigma_3}{\sigma_{\text{ref}}}\right)^{0.076}\left(\frac{d}{d_{\text{ref}}}\right)^{-0.098}v^{-0.309} \end{aligned}\right\} \tag{15}$$

The conversion formulas between macro cohesion c and micro cohesion c^* are

$$\left.\begin{aligned} c &= 0.13\left(\frac{E^*}{E_{\text{ref}}}\right)^{1.257}\kappa^{*0.079}c^{*0.388}\left(\frac{\sigma_3}{\sigma_{\text{ref}}}\right)^{-0.251}\left(\frac{d}{d_{\text{ref}}}\right)^{-0.269} \\ c^* &= (1.807\times10^6)\left(\frac{E}{E_{\text{ref}}}\right)^{-6.203}c^{1.565}\left(\frac{\sigma_3}{\sigma_{\text{ref}}}\right)^{-0.457}\left(\frac{d}{d_{\text{ref}}}\right)^{-0.013} \end{aligned}\right\} \tag{16}$$

The conversion formula between the macro internal friction angle φ and the micro internal friction angle φ^* are

$$\left.\begin{aligned} \varphi &= 3.36\left(\frac{E^*}{E_{\text{ref}}}\right)^{0.379}\kappa^{*-0.008}\varphi^{*0.259}\left(\frac{\sigma_3}{\sigma_{\text{ref}}}\right)^{-0.142}\left(\frac{d}{d_{\text{ref}}}\right)^{-0.149} \\ \varphi^* &= (4.417\times10^{-6})\left(\frac{E}{E_{\text{ref}}}\right)^{1.751}\varphi^{3.151}\left(\frac{\sigma_3}{\sigma_{\text{ref}}}\right)^{0.274}, \varphi^*<90° \end{aligned}\right\} \tag{17}$$
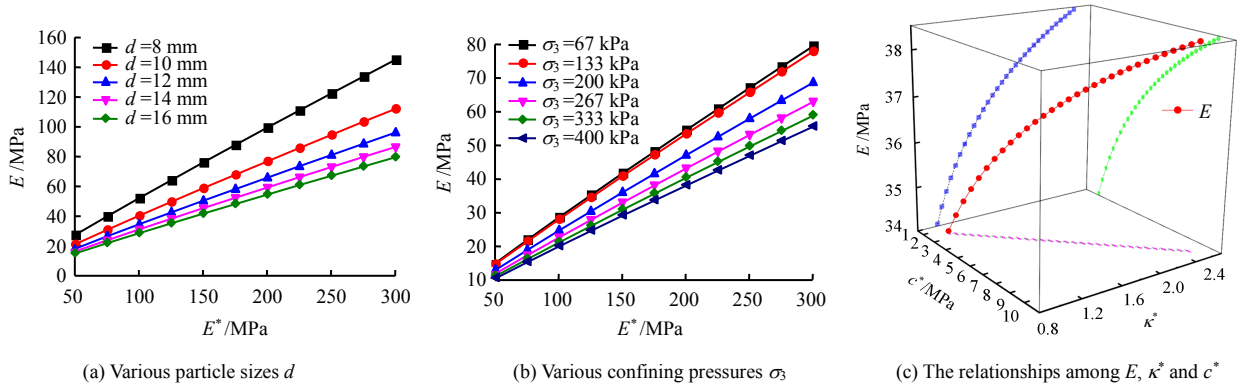
(a) Various particle sizes d (b) Various confining pressures σ_3 (c) The relationships among E, κ^* and c^*

Fig. 9   Relationships between Young's modulus and micro constitutive model parameters

(a) Various particle sizes d (b) Various confining pressures σ_3 (c) The relationships among v, E^* and c^*
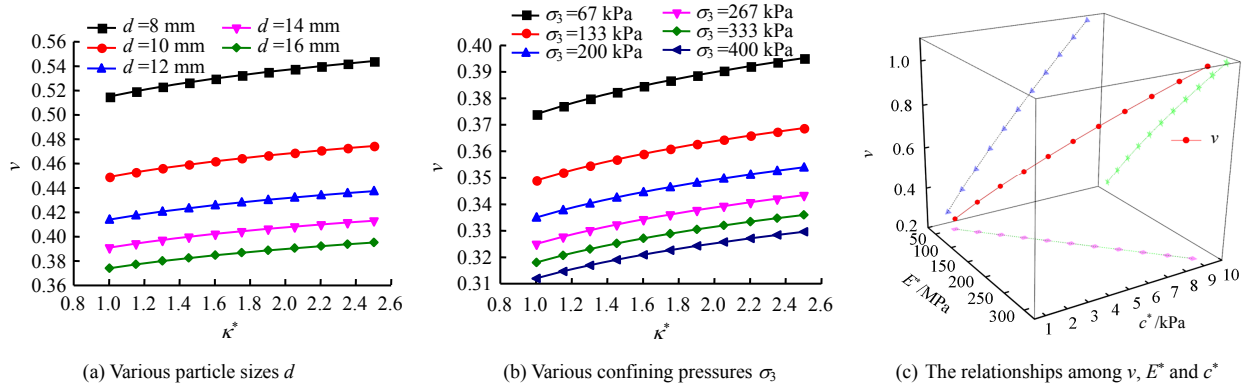
Fig. 10   Relationships between Poisson's ratio and micro constitutive model parameters

(a) Various particle size d (b) Various confining pressure σ_3 (c) The relationships among c, κ^* and E^*
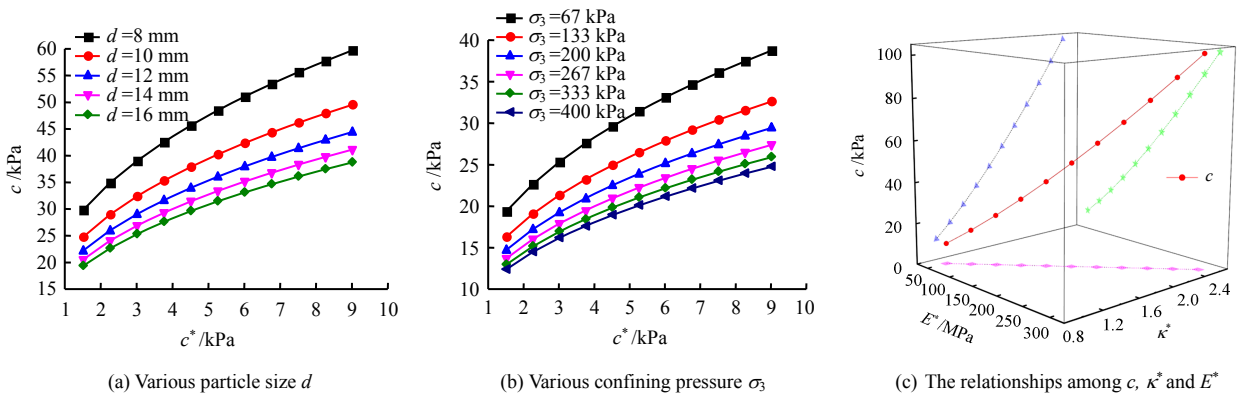
Fig. 11   Relationships between macro cohesion and micro constitutive model parameters

(a) Various particle sizes d (b) Various confining pressures σ_3 (c) The relationships among φ, E^* and κ^*
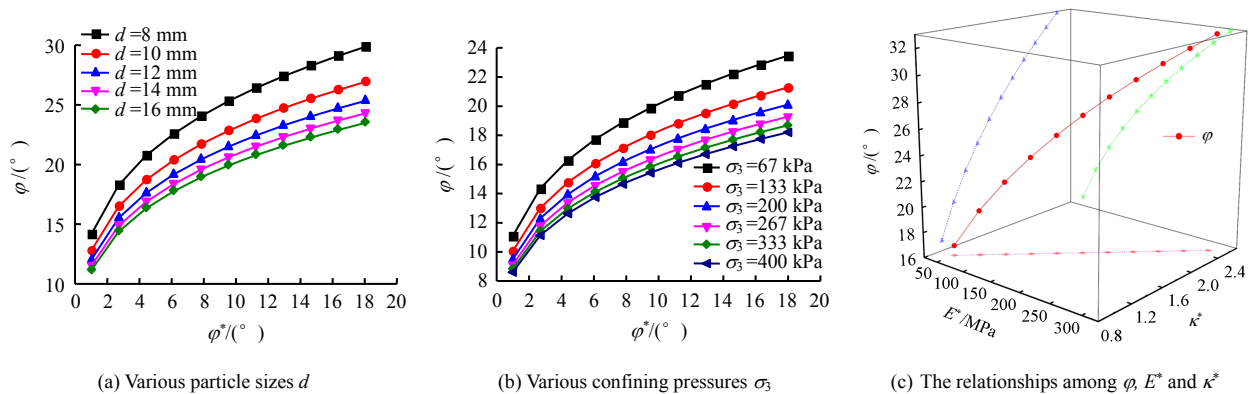
Fig. 12   Relationships between macro friction angle and micro constitutive model parameters

As shown in Figs.9−12, it indicates that the particle diameter d and confining pressure σ_3 have negligible effect on the macro Young's modulus E and the internal friction angle φ. They have effects on the macro cohesion c and the Poisson's ratio v to the greatest extent. The stiffness ratio κ^* bears a linear correlation with the effective modulus E^* and the micro cohesion c^*. The Young's modulus E has a non-linear relationship with the micro cohesion c^* and the stiffness ratio κ^*. As the micro cohesion c^* and stiffness ratio κ^* increase, the macro Young's modulus E increases with a deceasing growth rate. The correlation between other parameters is between linear and nonlinear.

Based on the conversion formulas, i.e., Eqs. (14)−(17), the micro model parameters can be estimated by the macro model parameters, which are implemented in FLAC³ᴰ 6.0 via the Fish programming. The input macro model parameters are obtained according to the field survey and engineering judgement.

4.4 Validation of the conversion formulas

The conversion formulas between the macro and micro model parameters are validated by the PFC³ᴰ simulation of cone penetration tests. The micro model parameters of the ②₁ layer of silty clay and the ⑤₁₋₁ layer of gray clay are estimated as shown in Table 5, by the macro model parameters listed in Table 1 and the proposed conversion formulas, i.e., Eqs. (14)−(17).

Table 5　Micro constitutive model parameters

Soil layer	E^*/MPa	κ^*	c^*/kPa	φ^*/(°)
②₁ silty clay	3.700	0.886	2.028	12.66
⑤₁₋₁ gray clay	3.831	0.577	8.696	6.368

PFC³ᴰ software was used to simulate cone penetration

test, and the cone resistance and sleeve friction were obtained. The simulation results were compared with the cylindrical cavity expansion theory-based solutions and CPT measurements in order to validate the conversion formulas between macro and micro model parameters. The dimensions of the PFC³ᴰ numerical model is the same as that of the numerical model for cone penetration test. The cylindrical numerical model has a radius of 0.38 m and a height of 1 m. The sizes of the penetrometer are the same as those listed in Table 3. According to reference [23], the particle diameters range from 9 to 15 mm, and the fluid−solid coupling effect is not considered.

When Eqs. (5) and (13) are used to estimate the cone resistance and sleeve friction, the information on the friction coefficient μ between the soil and the friction sleeve is required. The friction coefficient is back-calculated based on the in-situ CPT data (see Table 2) in combination with Eqs. (5) and (13). Thus, the cavity expansion theory-based solutions of cone resistance and sleeve friction can be derived according to the geotechnical parameters given in Table 1.

The theoretical values of the cone resistance and sleeve friction estimated by the cavity expansion theory and the PFC³ᴰ simulation results are summarized in Table 6. It can be concluded that the PFC³ᴰ simulation results are more close to the CPT data than the theoretical solutions. The maximum error of PFC³ᴰ simulation results in ⑤₁₋₁ layer of gray clay is 13.11%. Therefore, the conversion formulas between macro and micro model parameters developed by the cone penetration test modelling on the ②₁ layer of silty clay can be applicable to Shanghai clay or silty clay.

Table 6　Comparison between theoretical solutions, PFC3D simulation results and CPT data

Soil layer	Cone resistance					Sleeve friction				
	Measured mean /MPa	Cavity expansion theory-based solution /MPa	Theoretical error /%	PFC³ᴰ simulation results /MPa	Simulation error /%	Measured mean /kPa	Cavity expansion theory-based solution /kPa	Theoretical error /%	PFC³ᴰ simulation results /kPa	Simulation error /%
②₁ silty clay	0.67	0.673	0.45	0.726	8.35	25.9	25.7	0.77	28.5	10.89
⑤₁₋₁ gray clay	0.74	0.798	7.84	0.810	9.46	12.2	11.9	2.45	13.8	13.11

Note: The theoretical error of cavity expansion refers to the error between the theoretical value of cavity expansion and the measured average value; the calculation error of PFC³ᴰ is the error between the calculated result of PFC³ᴰ and the measured mean value.

Through the macro and micro coupling simulation, the cavity expansion theory-based solutions, the macro and micro coupling simulation results are discussed in the next subsection from the prospective of soil's macro continuous and micro discontinuous mechanical behavior during the cone penetration process.

4.5 Results interpretation from the macro prospective

4.5.1 Cavity expansion theory-based solutions

Based on the in-situ cone penetration test results

summarized in Table2, i.e., $q_c = 0.67$ MPa, $f_s = 25.9$ kPa, the friction coefficient $\mu = 0.042$ can be back-calculated by Eqs. (5) and (13). Thus, the cavity limit pressure $p_a = 0.62$ MPa can be obtained by Eq. (5) or (13). According to the geotechnical parameters listed in Table1, the cavity expansion theory-based solutions are shown in Table 7. It indicates that the errors of the cavity limit pressure, cone resistance and sleeve friction estimated by the cylindrical (cone) cavity expansion

theory compared with the in-situ CPT measured values   are 1.30%, 0.45% and 0.77%, respectively.

Table 7 Cavity expansion theory-based solutions of cone penetration test

Soil layer	Cavity limit pressure p_a /MPa		Error /%	Cone resistance q_c /MPa		Error /%	Sleeve friction f_s /kPa		Error /%
	Back-calculated mean value	Theoretical value		Measured mean	Theoretical value		Measured mean	Theoretical value	
②₁ layer silty clay	0.62	0.612	1.3	0.67	0.673	0.45	25.9	25.7	0.77

4.5.2 Calculation results of coupled numerical method

The numerical simulation results on the ②₁ layer of silty clay are shown in Fig.13. The coupled numerical model is 1m high, and the downward penetration direction is taken as negative. The subsurface soil with the depth ranging from −0.30 m to −0.65 m, i.e., the relative depth h/D ranging from −8 to −18 (h is the penetration depth and D is the cone diameter) with stable CPT data is interpreted.

The numerical results of the CPT in the interpreted range are shown in Fig.13. As shown in Fig.13(a), the black dots present the coupled numerical simulation results of q_c. The red line, the left axis and the right axis are the mean, minimum and maximum in-situ measurement of q_c, respectively. The coupling simulation results of q_c are in good agreement with the CPT measurements. The histogram indicates the frequency distribution of the coupled numerical modelling results of q_c in the interpreted range, which is characterized by a normal distribution. Figs. 13(b) and 13(c) demonstrate that the coupling simulation results of f_s and u are also consistent with the mean measured value. The coupling numerical modelling results of f_s are slightly higher and tend to increase as the depth increases, and its frequency distribution range is wider. The coupling numerical modelling results of u are slightly lower, which is characterized by a normal distribution.

The coupled numerical modelling results in Fig. 13 and the estimated cavity limit pressure are summarized in Tab.8. It indicates that the errors between the cavity limit pressure, cone resistance, sleeve friction and pore pressure and the measured values are 9.68%, 2.99%, 9.34% and 8.42%, respectively. The macro and micro coupling numerical simulation results are closer to the measurements than the cylindrical (cone) expansion theory-based solutions. In addition, the effect of pore pressure can be simulated.
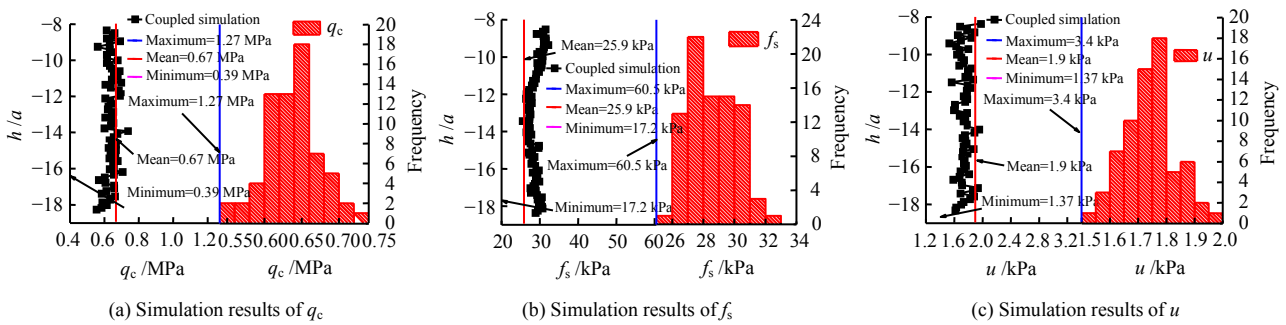

(a) Simulation results of q_c (b) Simulation results of f_s (c) Simulation results of u

Fig. 13 Results of the macro and micro coupling simulation

Table 8 Numerical simulation results of cone penetration test

Soil layer	Cavity limit pressure p_a /MPa			Cone resistance q_c /MPa			Sleeve friction f_s /kPa			Pore pressure u /kPa		
	Mean	Maximum	Minimum	Mean	Maximum	Minimum	Mean	Maximum	Minimum	Mean	Maximum	Minimum
②₁ layer silty clay	0.56	0.58	0.52	0.65	0.74	0.55	28.32	32.02	25.33	1.74	1.97	1.52

4.5.3 Distribution of plastic zone

During the cone penetration process, the change in the distribution of yielding elements in a given section is presented in Fig.14, which includes eight successive states. The given section is at a relative depth h/D of −11.11. On the right-hand side of each figure, the relative position of the CPT penetrometer and the given section during the cone penetration is shown.

Figures 14(a)−14(c) show that before the cone tip arrives, the tension zone (elements in pink) appears. As the cone gradually approaches, the tension zone increases. When the cone tip reaches the given section, the shear-induced yielding begins to occur in soils surrouding the cone and a plastic zone (elements in red) forms. The initial range of the plastic zone is encompassed by the white dashed circle in Fig.14(e). As the penetration

continues, the extent of the plastic zone gradually increases, and stress state of the elements surrounding the cone are gradually transformed from shear yielding state into historical shear yielding state (elements in cyan) as shown in Figs.14(e)−14(h). This finding is different from the change in the plastic zone estimated by the cyclindrical cavity expansion theory, where the plastic zone remains once the cavity expansion creases.

Because the macro and micro coupling simulation considers the interaction between the penetrometer and the surrounding soil particles.

4.6 Results interpretation from the micro prospective

The interpretation from the micro prospective includes the displacement of the soil surrounding the cone, the elastic-plastic boundary, the contact force chain and the stress distribution.
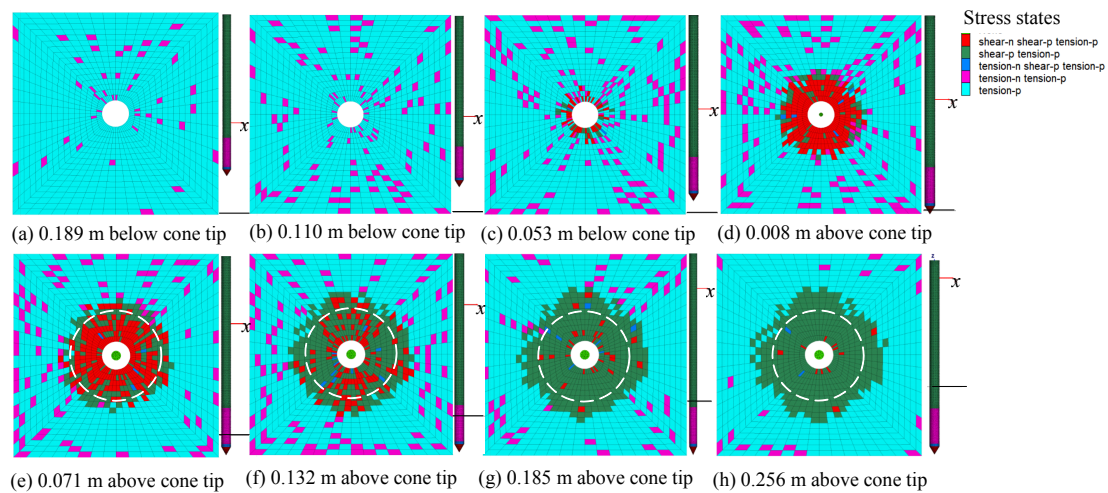

(a) 0.189 m below cone tip   (b) 0.110 m below cone tip   (c) 0.053 m below cone tip   (d) 0.008 m above cone tip

(e) 0.071 m above cone tip   (f) 0.132 m above cone tip   (g) 0.185 m above cone tip   (h) 0.256 m above cone tip

Fig. 14 Stress states of soil elements at the specific section with various elevations relative to the penetrating cone

4.6.1 Soil displacement and elastic-plastic boundary

When the relative depth h/D varies from −8 to −18, the simulated cone penetration data is relatively stable. The soil radial displacement contours surrounding the penetrometer in the vertical section is shown in Fig.15(a), which are in the shape of a "bud". The soil particles adjacent to the penetrometer have the greatest displacements, while the soil particles far away from the penetrometer and those below the cone tip have smaller displacements. The maximum displacement occurs at the junction of the continuous solid elements and discrete particles on the upper part of the friction sleeve. The soil is continuously squeezed when the cone penetrates into the soil. The radius of the squeezing zone $r = 0.16$ m , which is about 4.4 times the diameter of the cone.

The circular radial displacement contours in the horizontal section at a relative depth h/D of −13.9 are shown in Fig.15(b). It can be found that the particles near the penetrometer have the greater radial displacement, and those far away have smaller radial displacements. The radial displacement contours in the continuous element are circular and decrease toward the periphery.

In the horizontal section shown in Fig. 15(b), the ratio of the radial displacement to the radial location u_r/r at the grid nodes in the *x*-direction and *y*-direction

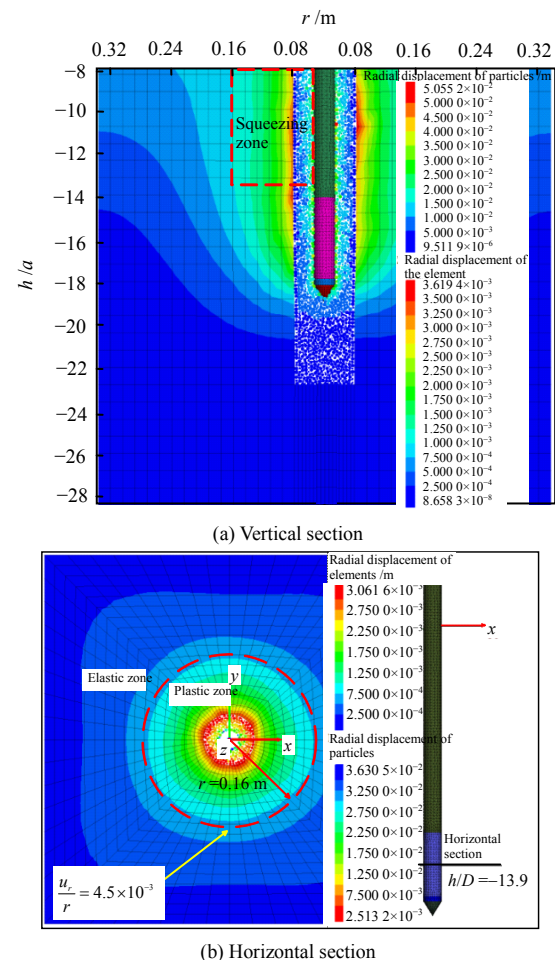(a) Vertical section

(b) Horizontal section

Fig. 15 Radial displacement contours of the soil around the penetrometer

are plot as the black and the red line as shown in Fig. 16, respectively. It can be found that the ratio decreases like a hyperbolic decline. By substituting the geotechnical parameters listed in Table 1 into Eq. (1), it can be found that the ratio u_r / r at the elastic-plastic boundary is $u_b / b = 4.5 \times 10^{-3}$. This cavity expansion theory-based value is indicated by the red dashed line at the radial location of $r = 0.16$ m in Fig. 15, which is consistent with the outer boundary of the squeezing zone. Then, when the radial location of the elastic-plastic boundary $b = 0.16$ m, the ratio u_r / r can be estimated by the cavity expansion theory which is plot as the blue line in Fig.16. It can be concluded that the coupling simulation results are consistent with the cavity expansion theory-based solutions.
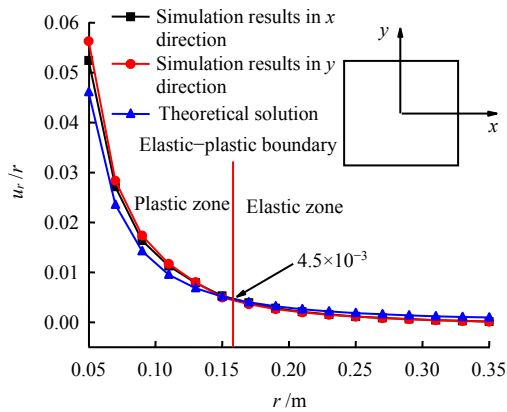

Fig. 16 Theoretical solutions and simulation results of radial displacements

4.6.2 Contact force chain and stress distribution

When the cone penetration data is stable, i.e., the relative depth ranges from −8 to −18, the soil force chain and radial stress distribution contours around the penetrometer in the vertical section are shown in Fig.17(a). During the cone penetration process, the force chain concentrates on the cone tip and the area surrounding the periphery. The greatest thickness of the force chain appears at the cone tip. The thickness of the force chain is positively proportional to the intensity of the contact force between particles. The force chain indicates the force transmission between the particles at a micro level. The stress distribution in continuous elements indicates that when cone penetration reaches a certain depth, the vertical stresses contour presents as a pear-shaped distribution, which is consistent with the Meyerhof theory-based solutions [24].

The radial force chain and stress distribution contours

of the soil around the penetrometer in the horizontal section at a relative depth h / D of −13.9 are shown in Fig.17(b). It indicates that the radial contact forces between the particles adjacent to the penetrometer reach the highest values. The particles far away from the penetrometer have lower radial contact forces. The stress distribution contours in the continuous element are circular and decrease toward the periphery. In the horizontal section shown in Fig. 17(b), the radial stress in the elements in the x-direction and y-direction are plot as the red and the blue line as shown in Fig. 18, respectively. When the radius is 1.6 times the radial location of the elastic-plastic boundary, the cavity expansion theory-based solution of the radial stress is slightly higher. The difference between the theoretical value and the simulation result is the largest at the elastic-plastic boundary with the difference of around 40 kPa. When the radial location is greater than 1.6 times the radial location of the elastic-plastic boundary, the coupling simulation results of the radial stresses remains unchanged, while the theoretical values decreases slowly. In whole, the coupling simulation results are in good agreement with the cavity expansion theory-based solutions.
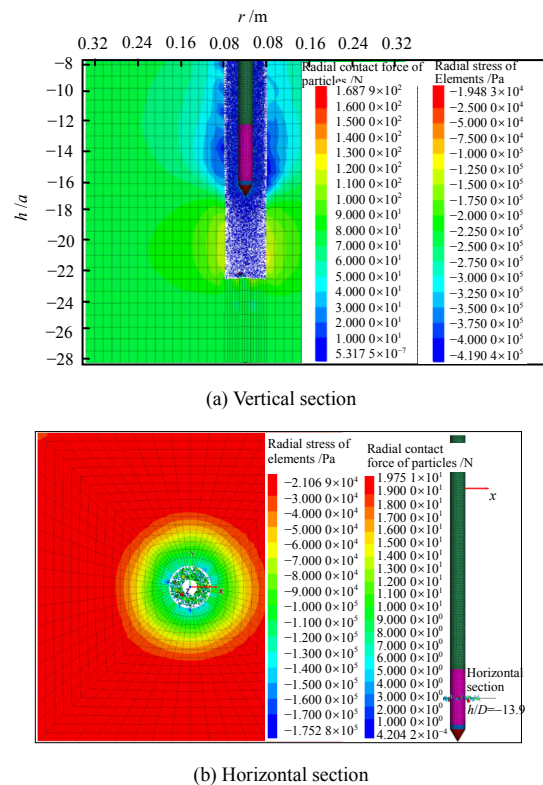

(a) Vertical section

(b) Horizontal section

Fig. 17 Force chain and stress distribution contours of the soil around the penetrometer
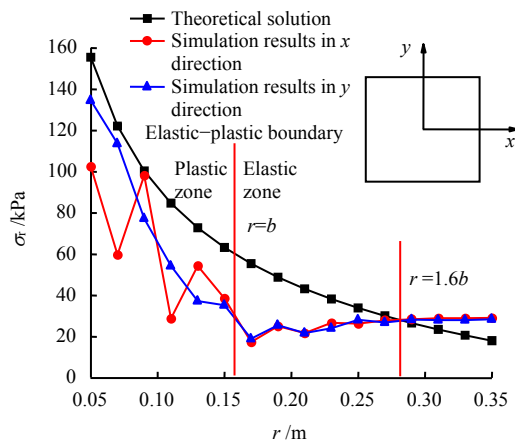
Fig. 18 Theoretical solutions and simulation results of radial stresses

5 Conclusion

(1) Based on the cylindrical (cone) cavity expansion theory in combination with the perfectly elastoplastic model with Mohr-Coulomb yield criterion, the static force equilibrium relationships are established, which relate the geotechnical parameters to the CPT measurements (i.e., cone resistance and sleeve friction).

(2) Using the macro and micro coupling mechanics approach, the conversion formulas that relate the macro Mohr-Coulomb perfectly elastoplastic model parameters to the micro linear parallel-bond model parameters are proposed considering the coupling mechanism, the selection of the macro and micro mechanical constitutive model and the parameter conversion. The conversion formulas are programmed in Fish and implemented in the commercial software FLAC^{3D}. The applicability of the macro and micro conversion formulas are verified through the PFC^{3D} modelling results which are in good agreement with the theoretical estimation and test data of CPT on the Shanghai ②$_1$ layer (silty clay) and the ⑤$_{1-1}$ layer (gray clay).

(3) Taking the CPT data on the shallow bearing layer, i.e., the ②$_1$ silty clay in a construction site in Gubei New Area, Shanghai, China as an example, the discrepancies between the theoretical solution, numerical modelling results and the CPT measurements of cone resistance, sleeve friction and cavity limit pressure are analyzed from a macro perspective. The discrepancies between the theoretical solutions and the CPT measurements of the cavity limit pressure, cone resistance and sleeve friction are 1.30%, 0.45% and 0.77%, respectively. The discrepancies between the macro and micro coupling simulation results and the CPT measurements of the cavity limit pressure, cone resistance, sleeve friction and pore pressure are 9.68%, 2.99%, 9.19% and 8.42%, respectively. It indicates that the macro

and micro coupling numerical modelling results are not only in agreement with the cylindrical (cone) cavity expansion theory-based theoretical solutions and the CPT measurements, but also the effect of pore pressure and the micro mechanical soil behavior can be simulated.

The proposed macro and micro coupling simulation method provides insight into the CPT mechanism and the approach to estimating the macro-micro parameters of geotechnical constitutive models.

References

[1] LIU Song-yu, WU Yan-kai. On the status of art and development of CPT in China[J]. Chinese Journal of Geotechnical Engineering, 2004, 26(4): 553−556.

[2] DUAN W, CAI G, LIU S Y, et al. Correlations between shear wave velocity and geotechnical parameters for Jiangsu clays of China[J]. Pure and Applied Geophysics, 2019, 176(2): 669−684.

[3] CHEN S L, ABOUSLEIMAN Y N. Exact undrained elasto-plastic solution for cylindrical cavity expansion in modified Cam Clay soil[J]. Géotechnique, 2012, 62(5): 447−456.

[4] QIU Min, YUAN Qing, LI Chang-jun, et al. Comparative study of calculation methods for undrained shear strength of clay based on cavity expansion theory[J]. Rock and Soil Mechanics, 2019, 40(3): 1059−1066.

[5] GENG Gong-qiao, CAI Guo-jun, DUAN Wei-hong, et al. Research on size effect and penetration rate of CPTU based on large deformation finite element[J]. Chinese Journal of Geotechnical Engineering, 2015, 37(Suppl.1): 94−98.

[6] AHMADI M M, DARIANI A A G. Cone penetration test in sand: a numerical-analytical approach[J]. Computers and Geotechnics, 2017, 90: 176−189.

[7] JIANG M, SHEN Z, WANG J. A novel three-dimensional contact model for granulates incorporating rolling and twisting resistances[J]. Computers and Geotechnics, 2015, 65: 147−163.

[8] ZOU Yu-xiong, MA Gang, LI Yi-ao, et al. Impact of rotation resistance on fabric of granular materials[J]. Rock and Soil Mechanics, 2020, 41(8): 2829−2838.

[9] DENG Yi-bing, YANG Yan-cheng, SHI Dan-da, et al. Optimization and application of variable particle size method in three-dimensional discrete element large-scale simulation[J]. Chinese Journal of Geotechnical Engineering, 2017, 39(1): 62−70.

[10] MA Y, SHENG Q, ZHANG G, et al. A 3D discrete-continuum coupling approach for investigating the deformation and failure mechanism of tunnels across an active fault: a case study of Xianglushan tunnel[J]. Applied Sciences, 2019, 9(11): 2318.

[11] LI Bo. Theoretical research on cavity expansion and its

application in cone penetration technology[D]. Dalian: Dalian University of Technology, 2007.

[12] Itasca Consulting Group, Inc. FLAC³ᴰ (fast Lagrangian analysis of continua in 3D) theory and background[R]. Minneapolis: Itasca Consulting Group, Inc., 2017.

[13] Itasca Consulting Group, Inc. PFC³ᴰ (particle flow code in 3D) theory and background[R]. Minneapolis: Itasca Consulting Group, Inc., 2014.

[14] LIU S, WANG J. Depth-independent cone penetration mechanism by a discrete element method (DEM)-based stress normalization approach[J]. Canadian Geotechnical Journal, 2016, 53(5): 871−883.

[15] YAO Yang-ping, HOU Wei, LUO Ting. Unified hardening model of soil[J]. Chinese Journal of Rock Mechanics and Engineering, 2009, 28(10): 2135−2151.

[16] GUI M W, BOLTON M D, GARNIER J, et al. Guidelines for cone penetration tests in sand[C]//Centrifuge. Rotterdam: A. A. Balkema, 1998.

[17] JIANG M J, YU H S, HARRIS D. Discrete element modelling of deep penetration ingranular soils[J]. International Journal of Numerical and Analytical Methods in Geomechanics, 2006, 30(4): 335−361.

[18] ABI Erdi, ZHENG Ying-ren, FENG Xia-ting, et al. Relationship between particle micro and macro

mechanical parameters of parallel-bond model[J]. Rock and Soil Mechanics, 2018, 39(4): 1289−1301.

[19] YOON J. Application of experimental design and optimization to PFC model calibration in uniaxial compression simulation[J]. International Journal of Rock Mechanics and Mining Sciences, 2007, 44(6): 871−889.

[20] CHEN Jian-feng, LI Hui-li, ZHOU Jian. Study on the Relevance of macro-micro parameters for clays[J]. Chinese Quarterly of Mechanics, 2010, 31(2): 304−309.

[21] ZHOU Bo, WANG Hua-bin, ZHAO Wen-feng, et al. Analysis of relationship between particle mesoscopic and macroscopic mechanical parameters of cohesive materials[J]. Rock and Soil Mechanics, 2012, 33(10): 3171−3178.

[22] SU Hui, YANG Jia-qi, HU Bao-wen, et al. Study of particle size effect of rock model based on particle discrete element method[J]. Rock and Soil Mechanics, 2018, 39(12): 4642−4651.

[23] ARROYO M, BUTLANSKA J, GENS A, et al. Cone penetration tests in a virtual calibration chamber[J]. Géotechnique, 2011, 61(6): 525−531.

[24] MEYERHOF G G. Ultimate bearing capacity of footings on sand layer overlying clay[J]. Canadian Geotechnical Journal, 1974, 11(2): 223−229.